



Co-funded by the Walloon region



12.2.2 Deliverable – Geophysical imaging pre-sampling report

(Les Champs Jouault landfill)

Date: August, 2019



SUBJECT: WPI2 Report of pre-sampling geophysical investigation on pilot landfill 2

report
 information
 consideration
 decision

To: ... **From:** BGS & ULiege

Introduction

The following report describes the results of the first geophysical survey carried out on the landfill of Les Champs Jouault, located in the Manche department in Normandy, France (Fig. 1). This landfill is the second RAWFILL pilot sites chosen to demonstrate the use of geophysical methods as part of a standard framework assessment of enhanced landfill mining projects.

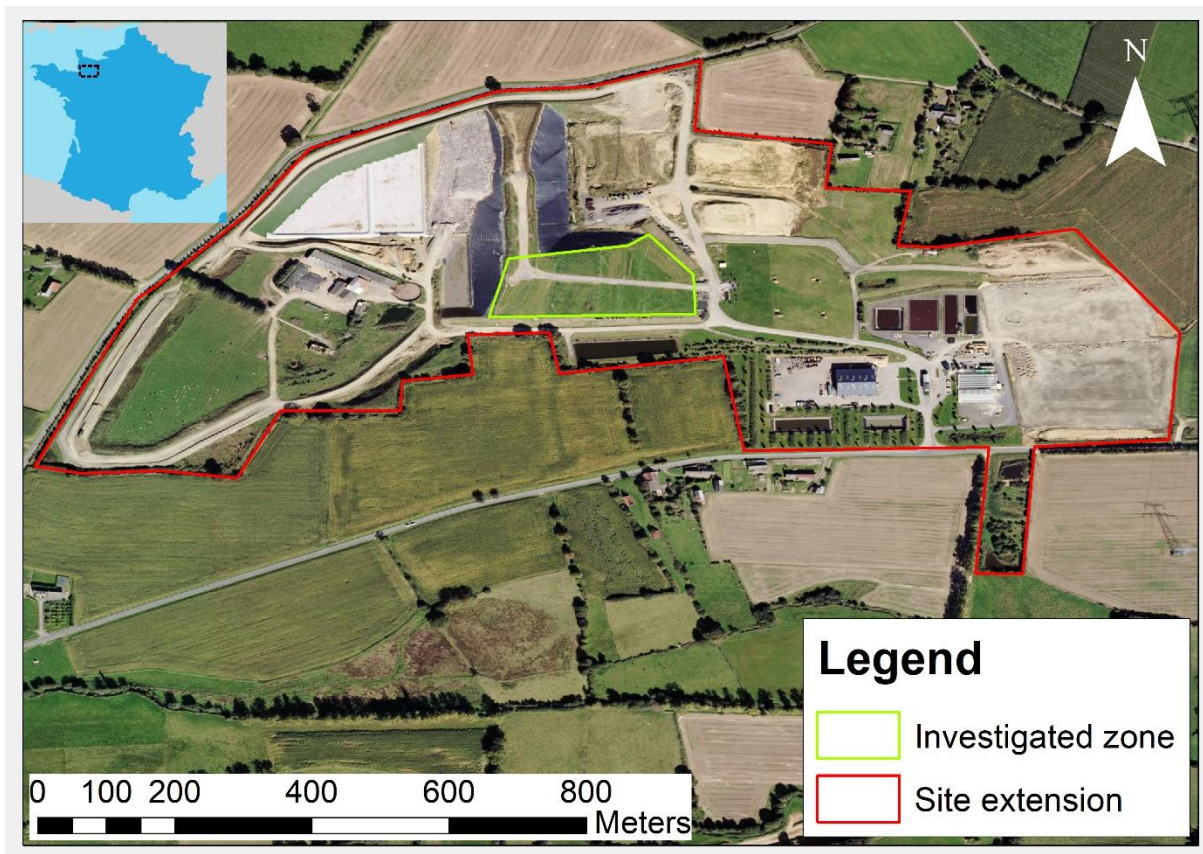


Figure 1: Les Champs Jouault site (in red) and the investigated area (in green).

For the first survey, we decided to apply a combination of different geophysical methods in order to characterize the four oldest waste cells of the landfill. The purpose of the characterization is double. First, we want to highlight zones of the landfill that represent interesting features possibly related to parameters of interest such as high metallic content. In a second step, based on identified zones, the idea is to point out some locations for sampling (either by drilling or trenching) that will be carried out by the SAS Les Champs Jouault. The correlations between the geophysical results and the data collected during sampling will then be analysed in order to validate and calibrate geophysical models. Finally, the correlation analysis will serve as basis to establish a resource distribution model for the landfill.

The geophysical survey was conducted by the University of Liege (Uliege) and the British Geological survey (BGS) from November 12th to 15th 2018. It was arranged in close coordination with SAS Les Champs Jouault and planned based on the Remote Imaging Report (D2.1.2). The geophysical survey design is discussed in the Survey Design Report (D2.2.1). Although, the described survey design had to be slightly modified due to practical issues on site.

Summary of the study area

The landfill of Les Champs Jouault is operational since 2009. It is a non-hazardous municipal solid waste landfill (MSWL) equipped with a leachate recirculation system and operated as a bioreactor. The composition of incoming waste is approximately 50% household waste and 50% non-hazardous industrial waste. The landfill is divided in several cells. Their dimension is approximately 100 m long, 50 m wide and 15 m thick at their maximum height. The vertical structure of a cell is composed of distinct layers as visualized in Figure 2. The layering of the cells comprises a 1 m soil cover overlaying a 10-15 m thick layer of waste. The bottom of the cells consists of a 0.5 m layer of draining materials. To maximize biogas extraction and to reduce environmental risk, the whole cell structure is double sealed with a clay layer as a passive barrier and an HDPE geomembranes as an active barrier (see Figure 2A).

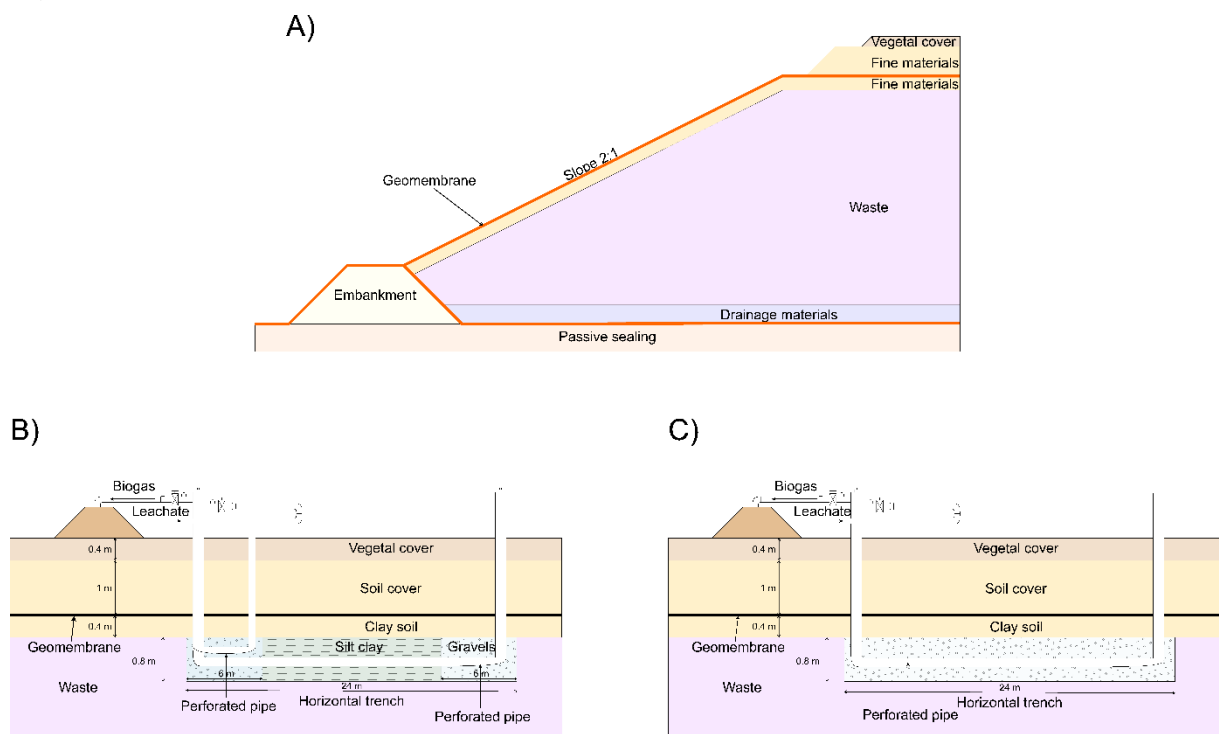


Figure 2: General cross-section of a cell in Les Champs Jouault (A) (modified from Grossin-Debattista et al., 2014), biogas extraction and leachate recirculation systems in cells 3 (B) and 4 (C). The same pipes are used for biogas extraction and leachate injection (modified from Audebert et al. 2016).

For the biogas extraction and leachate recirculation, pipes are embedded in gravel filled trenches along the top of the waste layer. An example of the circulation system implemented in cells 2 and 3 is provided in Figure 2B and C, respectively. Figure 3 shows the setup on top of the cells.



Figure 3: Gas extraction and leachate recirculation system present on the landfill.

Geophysical investigations

Main investigation area

The geophysical survey was conducted over cells 1 to 4. They were chosen for several reasons. Firstly, these are the oldest cells present in the landfill (see closure dates in table 1). We can therefore assume that a certain level of mineralization already occurred in these cells. As they were closed at different times, they should nevertheless exhibit different mineralization states offering a good opportunity to verify if such a mineralization contrast can be detected with geophysical methods. A second reason is related to the different waste compositions of the cells, potentially resulting in a different geophysical signature (see Figure 5). Finally, cells 3 and 4 are already equipped with geophysical sensors (e.g. Audebert et al., 2016; Audebert et al., 2014; Grossin-Debattista et al., 2014) providing additional geophysical information over different periods of time.

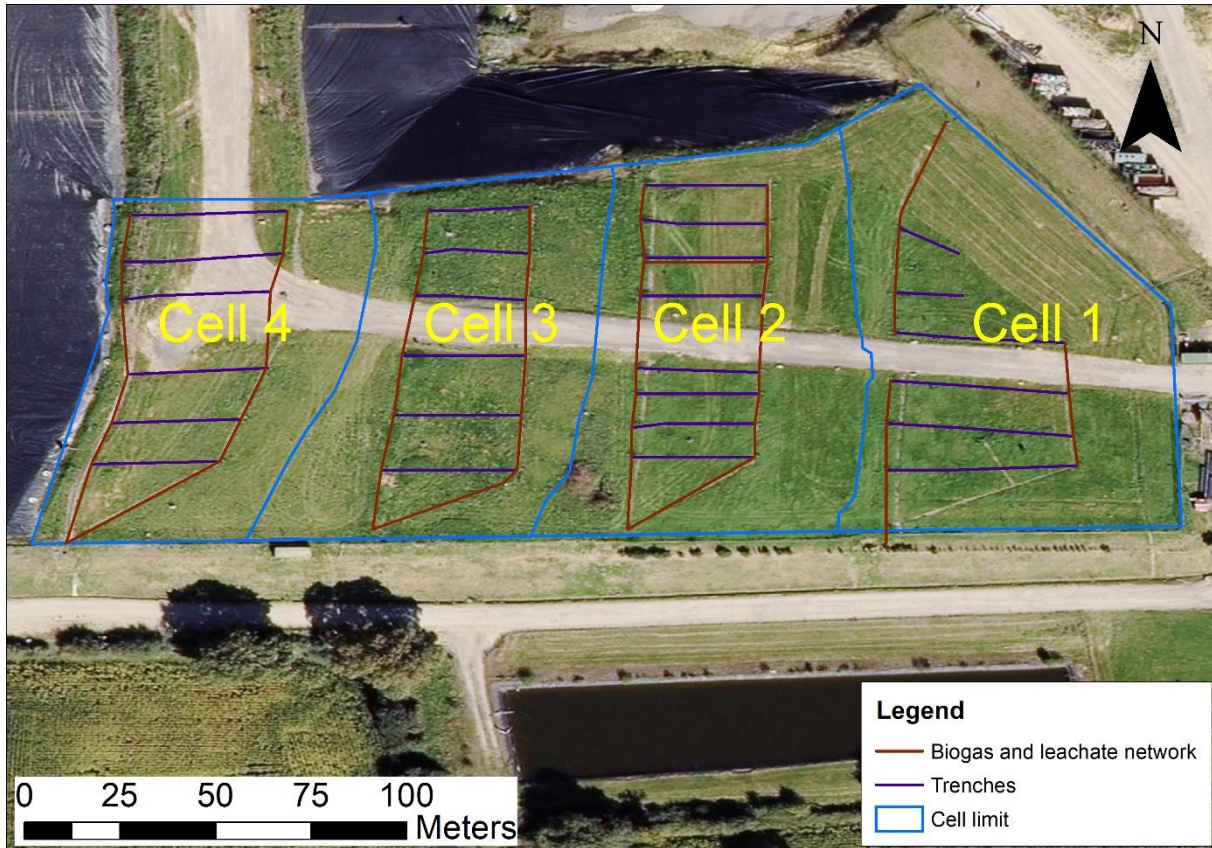


Figure 4: Study area with the cell limit and the biogas extraction and leachate recirculation network.

Cell 1 is the oldest and smallest cell investigated during the geophysical survey. It is of particular interest because it contains more industrial waste compared to the other cells (see Figure 5). Cells 2 and 3 are rather similar in terms of composition. Cell 4 contains almost only 3 types of waste (i.e. industrial, household and bulky wastes). In that, it differs from the other cells which contain a non-negligible amount of contaminated soil or shredder residue.

Table 1: Summary of the main characteristics of the investigated cells.

	Cell 1	Cell 2	Cell 3	Cell 4
Start date	April 2009	April 2010	January 2011	September 2011
End date	April 2010	January 2011	September 2011	July 2012
Mass of waste stored (in Tons)	36043	50385	61331	64333
Area (m²)	3404	4304	4302	4306
Geophysical instrumentation (IRSTEA)	/	/	ERT/IP (3 lines)	- ERT/IP (4 lines) - 4 optical fibers - 15 thermistors - 4 resistivity rakes

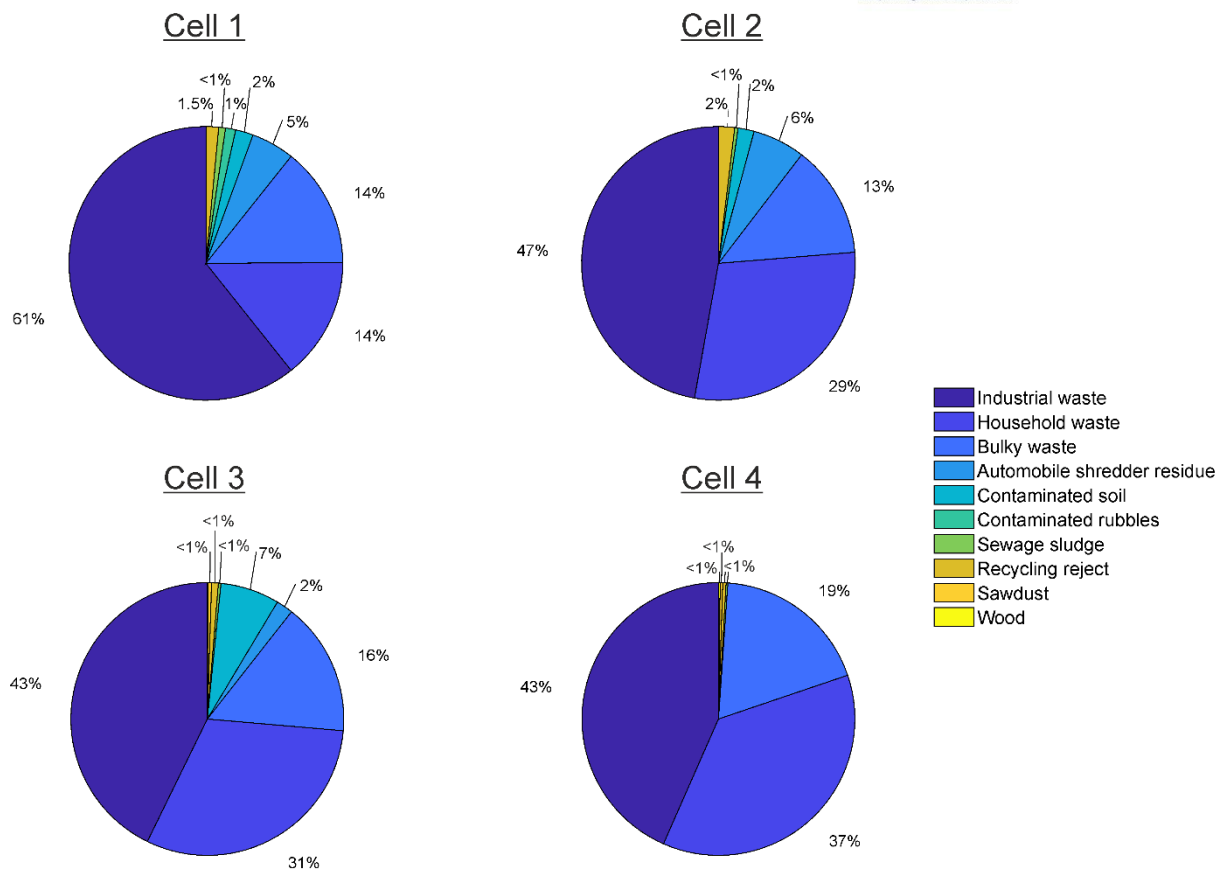


Figure 5: Distribution of waste stored in cells 1 to 4

Geophysical methods and coverage

In the following, all applied geophysical methods are listed with their expected main sensitivities on landfills. Different geophysical methods are sensitive to different physical properties and can therefore complement each other. For a more detailed description of each geophysical method, please refer to the following report T1.3.1: Swot analysis of LF characterization methods.

In order to get a full areal coverage, the following mapping methods were used:

- **Magnetic field mapping:** to identify zones with high metal content (measuring changes in total magnetic field/gradient)
- **Electromagnetic (EM):** to reveal lateral extent of different waste composition or leachate content at several distinctive depths (mapping changes in electrical conductivity and magnetic susceptibility)

More focused 2D surveys, providing detailed information about changes of physical properties with depth, were done along distinct profiles including the following methods:

- **Ground Penetrating Radar (GPR):** to measure the thickness of the cover layers (registering the returned GPR signal which was reflected or diffracted at material boundaries with significant changes in relative electric permittivity).
- **Horizontal to Vertical Noise Spectral Ratio (HVNSR):** to estimate the thickness of the landfill (measuring seismic velocities)
- **Multichannel Analysis of Surface Waves (MASW):** to characterize the shear wave velocity structure of the subsurface indicating layers of different waste composition and the transition to the host material (measuring seismic velocities)

The EM and Magnetic mapping were performed across the four cells on a grid formed of parallel, 4m spaced East-West oriented line (Figs. 6 and 7). For the Ground penetrating Radar several East West aligned lines were measured across all 4 cells (Fig. 8, bright blue lines). The HVNSR measurement were aligned with the northern and the southern MASW profiles (Fig. 8, orange dots). The MASW was measured along three profile lines in East-West direction across the cells (Fig. 8, dark blue lines).

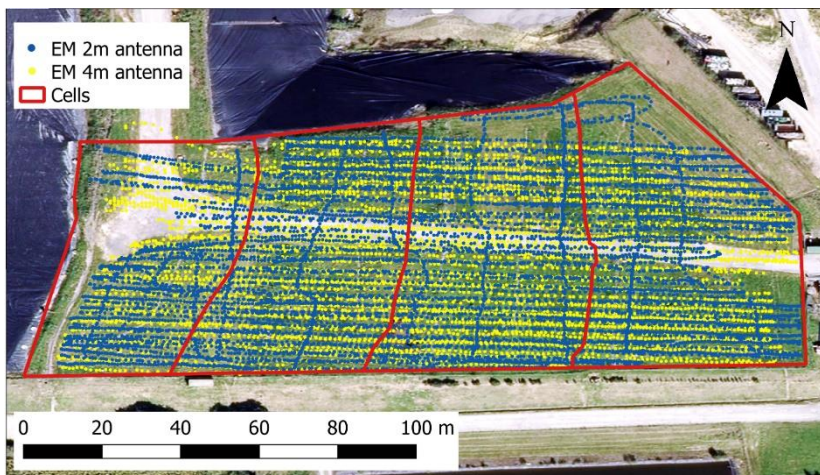


Figure 6: Extent of the Electro-magnetic mapping with the 2m antenna (yellow) and the 4m antenna (blue)

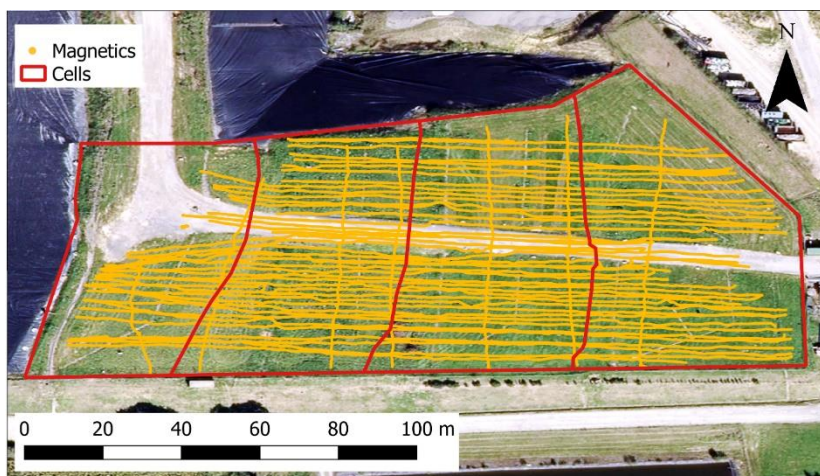


Figure 7: Extent of the Magnetic mapping

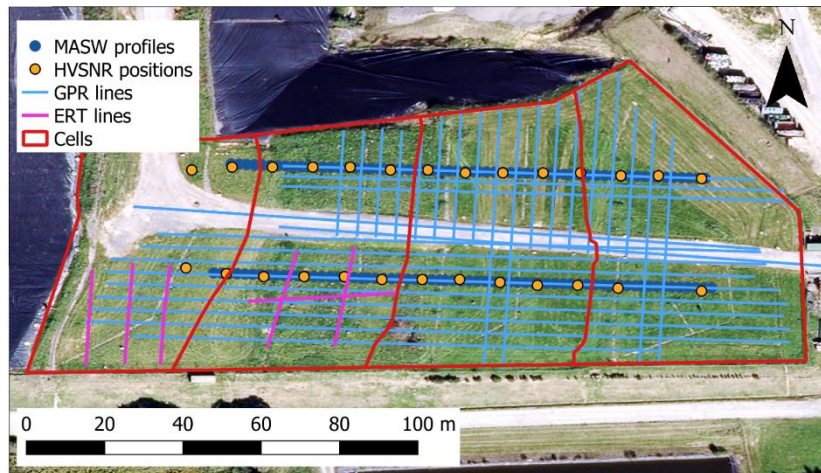


Figure 8: Location of GPR profiles (bright blue) and the MASW profiles (dark blue). The HVSNR measurements were aligned with the MASW profiles (orange dots). The ERT/IP profiles are displayed in purple. These lines are managed by IRSTEA.

ERT and IP measurements were not acquired during the field survey but were acquired later (in January 2019) by IRSTEA which is responsible of the electrical system installed (Fig. 8, purple lines). These methods are used to:

- **Electrical Resistivity Tomography (ERT):** to discriminate different waste types and investigate changes in leachate content (measuring resistivity distribution)
- **Induced Polarization (IP):** to detect metallic scraps or zones of higher organic content (measuring chargeability distribution)

Measurement systems and parameters

In the next section, the measurement parameters for each method are summarized.

The **electromagnetic** data was acquired using a conductivity meter model DUALEM-4. By attaching two different antennas sizes, mapping at four different depth levels could be achieved. These depths were 0.5 m and 2.3 m for the shorter antenna and 1.8 m and 5.3 m for the longer antenna. Both quadrature (related to apparent conductivity) and in-phase (related to apparent magnetic susceptibility) components were recorded simultaneously for each antenna. In addition, a GPS sensor (no RTK) was connected to the system for positioning (see Figure 9C and D).

The **magnetic** data were acquired with a portable caesium magnetometer model G-858 from Geometrics. All data were recorded in vertical gradient mode with 1 m separation between sensors and 0.6 m above ground level. The system was mounted on a cart as shown in Figure 9F. For positioning, all data were continuously synchronized with a GPS system (no RTK). To identify drifts in the magnetic data, a three-axis fluxgate magnetometer, FGM3D from Sensys, was setup as a base station at a position away from any visible disturbances.

Several **Ground Penetrating Radar (GPR)** profiles were acquired with a Pulse-EKKO Noggin system using a 250MHz antenna, which represents a good compromise between depth of investigation (to detect the covering membrane at the top of the waste) and resolution (to detect individual thin layers comprising the engineering capping layers). The antennas were mounted to a cart as shown in Fig. 9E. Georeferencing was achieved using an odometer wheel, marking survey reference points onto the data files that were then captured using the Leica Viva RTK GPS system deployed at site.

The method of **Horizontal to Vertical Noise Spectral Ratio (HVNSR)** was applied along the seismic profile lines by recording ambient seismic noise during 20 to 30 minutes at discrete locations. Data were recorded in the three components (vertical, north-south, east-west directions) using a seismometer LE-3Dlite MkIII with eigenperiods of 1s and upper frequency limit of 100 Hz. The location of the HVNSR station is shown in Fig. 9B.

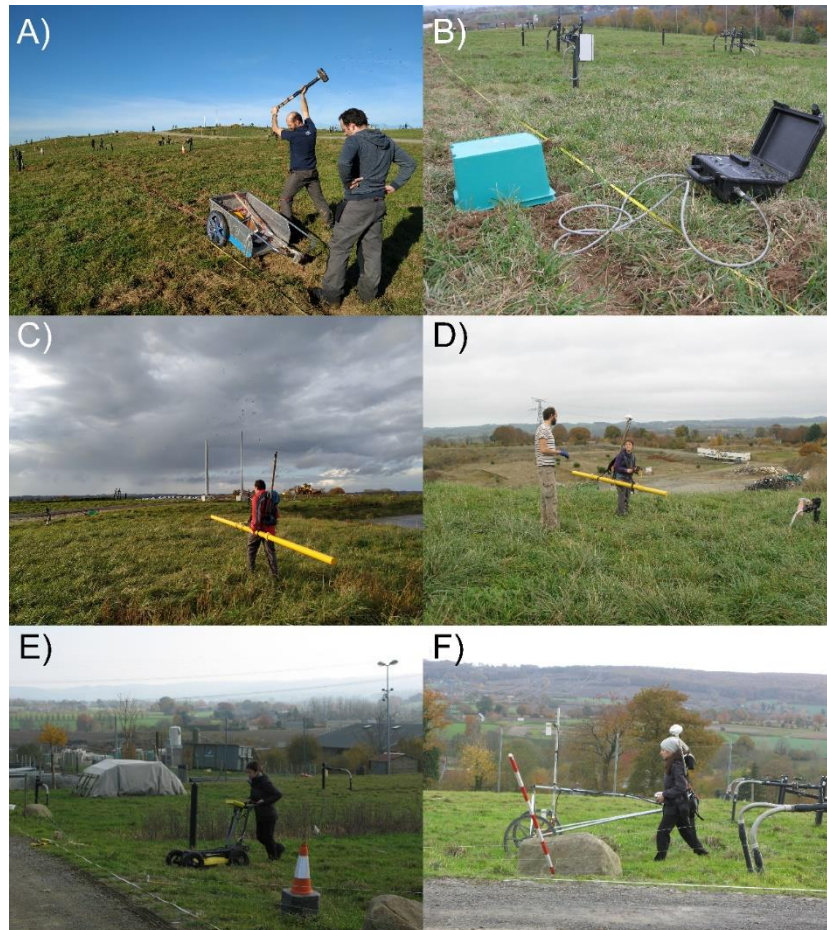


Figure 9: Acquisition of A) MASW, B) HVNSR, C) EM with long antennas, D) EM with short antenna, E) GPR and F) magnetic data on the landfill.

The **seismic** data was acquired using a Geometrics Geode Seismograph, utilising a towed geophone streamer deployed from a wheelbarrow (Fig. 9A). The streamer consisted of 24 vertical geophones (4.5Hz natural frequency), mounted on ground-coupled base plates at 1m centres and connected by woven kevlar reinforced webbing. A 5kg sledgehammer and ground-coupled striking plate was used as a seismic energy source, with the source located 2m ahead of the geophone streamer. In order to increase the signal to noise ratio (SnR), a total of three hammer blows were stacked at each shot location. It should be noted that the processed (1D) velocity sections derived from the MASW processing relate to a position equivalent to the mid-point of the geophone streamer (Fig. 8).

Electrical resistivity tomography (ERT) and time-domain induced polarization (TDIP or IP) data were acquired by IRSTEA with a Syscal Pro (Iris Instruments). Only cells 3 and 4 are equipped for ERT and IP measurements (see Fig. 10). In cell 3, three lines of 24 stainless steel electrodes were installed in November 2011 in three trenches dug in the clay layer installed just above the waste before the HDPE

geomembrane cover was laid. The spacing between the electrodes varies from 1 to 2.5 m. In cell 4, three lines of 24 electrodes were installed in October 2012 in three trenches dug in the clay layer above the waste before its covering with a HDPE geomembrane. The fourth line (also containing 24 electrodes) had been installed about 1 year earlier above 4 m of waste (Grossin-Debattista et al., 2014). The spacing between the electrodes of the top lines is 1.5 m whereas the electrodes buried into the waste are spaced by 2 m. The electrode setup is illustrated in Fig. 10. The acquisition sequence used differs from cell 3 to cell 4 but combines different electrical arrays in order to maximize the information provided. Collected data were inverted with BERT (Günther et al., 2006; Rücker et al., 2006). Model obtained with BERT satisfies the error weighted chi-square, $\chi^2 = 1$, meaning that the data were fitted to their error level.

We refer to Grossin-Debattista et al. (2014), Audebert (2015) and Jouen (2018) for more details about the acquisition and inversion setups used.

Electrode configuration

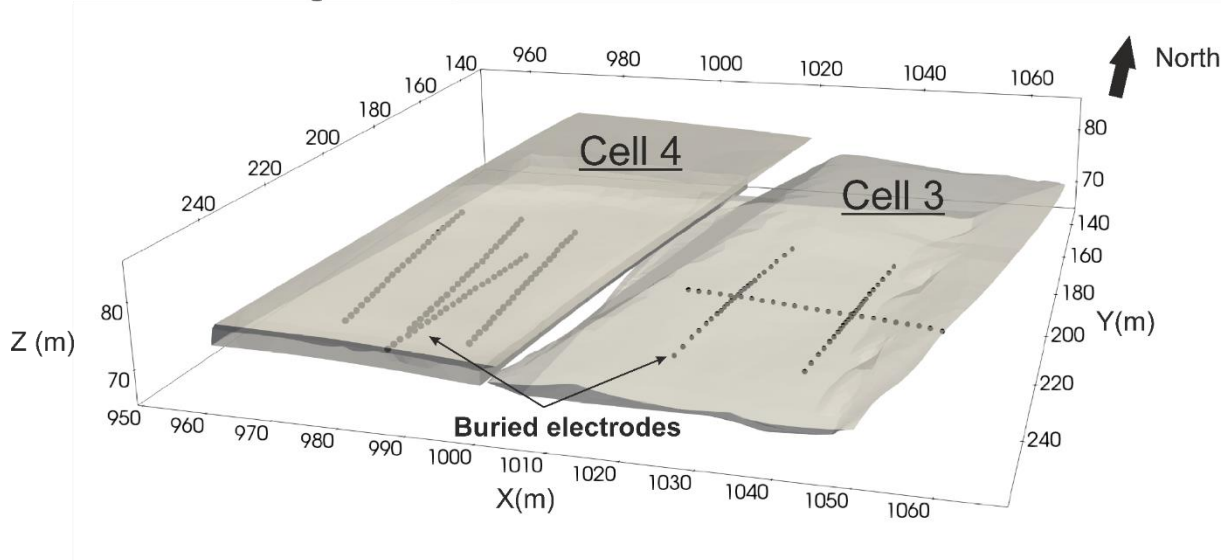


Figure 10: Electrode configuration in cells 3 and 4

Geophysical processing and results

The processing of data and results of each geophysical method are described in the following section. A summarizing conclusion at the end of the section discusses the overall interpretation with respect to the landfill characterization.

Magnetics

The first step in the magnetic data processing is to perform a correction for time variations of the magnetic field. Thanks to a base station which was setup outside the waste deposit area, such variations could be monitored throughout the magnetic survey on the landfill. Variations observed are provided in 11. The magnetic field acquisition was made in two phases between which measurements at the base station were stopped, explaining the gap in the data. A variation of 25 nT was observed between the two phases. During the magnetic survey, the variations were more limited (for example, only 17 nT variations during the second phase of acquisition). Such variations are small and only impact minimally the results. Magnetic field measured at the base station was nevertheless subtracted from the survey data acquired in the landfill.

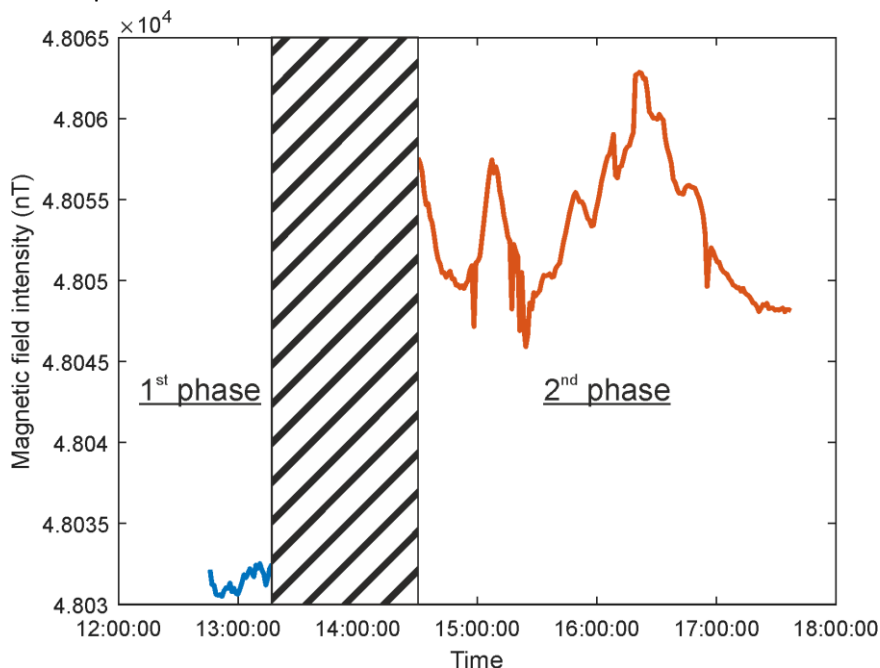


Figure 11: Variation in total magnetic field intensity during the magnetic survey in the landfill (which was divided in two phases)

Figure 12A shows a map of the total magnetic field measured in cells 1 to 4 whereas Figure 12B shows the vertical magnetic gradient covering the same area. The maps were obtained after a linear spatial interpolation of individual observation points. As explained in a previous section, the magnetic data are acquired with two sensors aligned vertically that are spaced by 1 meter. The displayed total magnetic field corresponds to the mean magnetic field measured by the two sensors (time variations are corrected). Therefore, red and blue colors in the map correspond to magnetic field anomalies. The vertical magnetic gradient map in Figure 12B represents the difference between the magnetic field measured at the two sensors. The vertical magnetic gradient is more sensitive to near-surface magnetic objects.

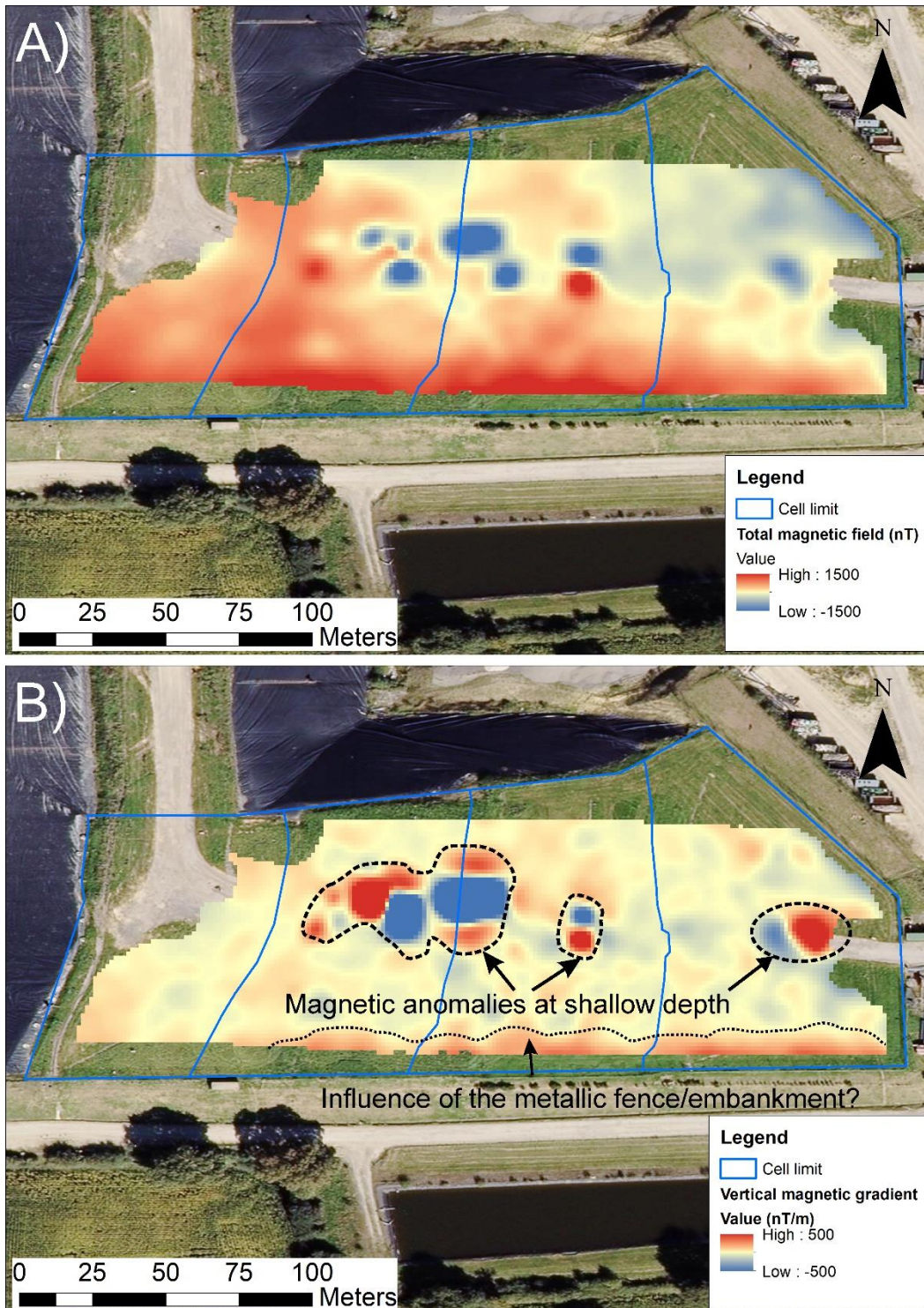


Figure 12: Maps of total magnetic field (A) and vertical magnetic gradient (B). Several magnetic anomalies are present on both maps. They are likely related to shallow magnetic structures (gas extraction or leachate recirculation network).

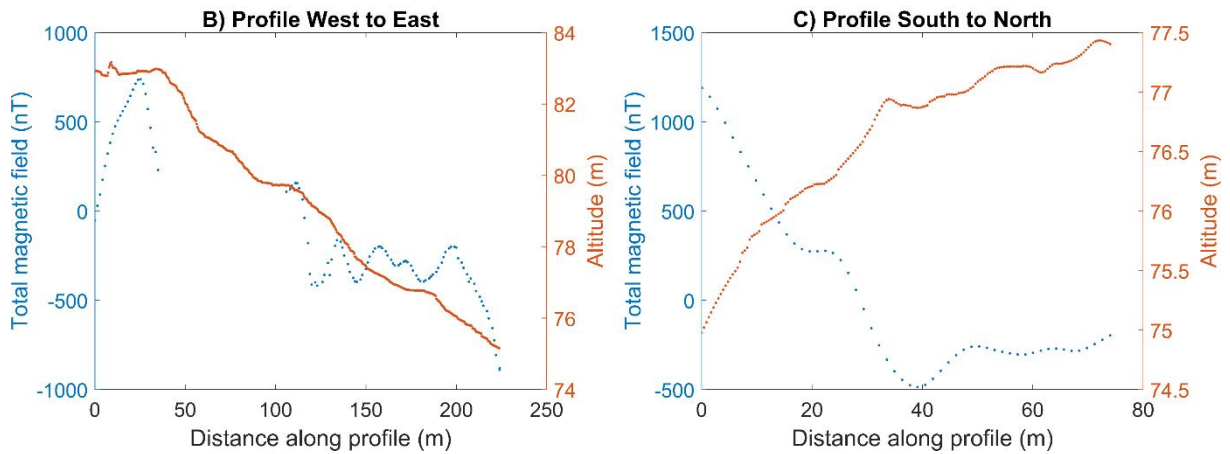
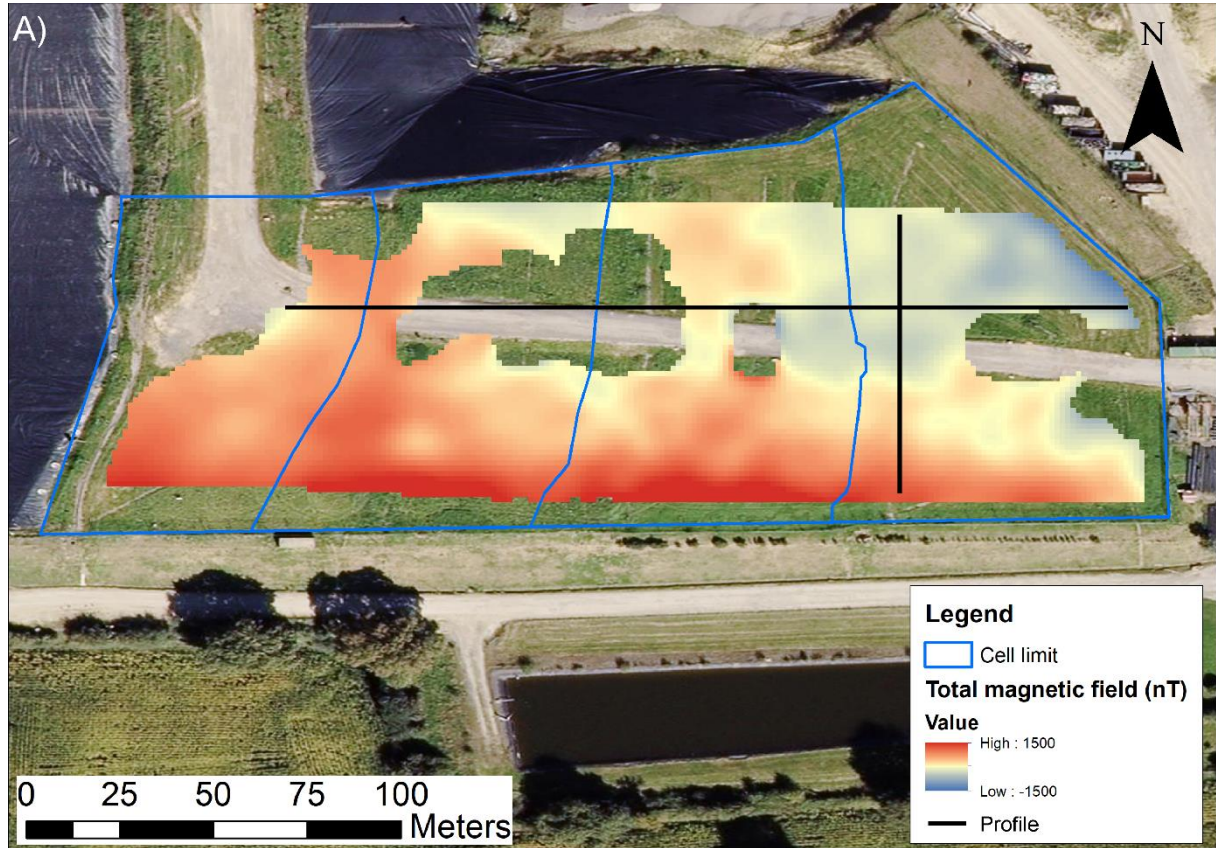


Figure 13: Magnetic profiles across the investigated area. A) Total magnetic field map where strong magnetic anomalies in the center (associated to near-surface structures) were removed. The locations of the magnetic profiles (B and C) are shown as black lines. B) and C) show the magnetic field and topography along the profiles oriented respectively from West to East and from South to North.

Several strong anomalies are present in both maps. Because their amplitude is large in the vertical gradient map, they probably correspond to metallic infrastructures present at shallow depth (possibly related to the gas extraction and/or leachate recirculation network or material composing the embankment) or at surface (metallic fence). These anomalies are identified by dashed polygons in Figure 12B. If we disregard them for the analysis of the total magnetic field map, a general trend still arises (Figure 13A). The magnetic field is higher in the southern and western parts of the investigated zone than it is on the rest of the map. This is particularly visible if we look at profiles of magnetic field (Figure 13B and C). Looking at the profile oriented from West to East, the trend seems to be related to the topography and thus to the waste thickness. On the South to North profile, the relation is much less clear but may be influenced by the embankment/fence present in the southern part of the profile.

Electromagnetic mapping

Similar to the magnetic data, all individual data points were interpolated with IDW to produce maps. The quadrature-phase component of the induced magnetic field can be related to the electrical conductivity and the in-phase component to the magnetic susceptibility (e.g. Dumont et al., 2017). The data is sensitive to different depths depending on the antenna used, either 2 m or 4 m antenna, and the orientation of the coils. All maps with the conductivity data at the four different depths are displayed in Figure 14. All magnetic susceptibility data are shown in Figure 15.

Overall, the conductivity data shows a clear increase with depth. Especially at the shallowest investigation depth of 0.5 m, the conductivities are significantly lower compared to the other measured depth. Usually, the cover layer is associated with lower conductivities than the waste material. We can therefore assume that the lower conductivities at 0.5 m depths correspond to the cover layer which has a thickness of less than 1.8 m. Starting from 1.8 m depths, we can see that the increased conductivities correspond to the waste material. This is especially clear since the clay boundaries between the cells are very well defined with lower conductivities around the waste cells (see black dashed lines separating the waste material in yellow from the clay separations in blue). A lower conductive band also crosses the four cells at the center in East-West direction. This is the influence of the street crossing the cells (white dashed lines in Fig. 16).

Similar infrastructure related anomalies are also seen in the magnetic susceptibility maps. Very high magnetic susceptibility magnitudes are visible close to where a car was parked and near a container (see Fig. 17 dashed orange lines). At shallow investigation depths, additional anomalies crossing the street are seen in the magnetic susceptibility maps (Fig. 15 top figure). These might be metallic drainage tubes below the street.

Comparing the different cells, gives some indication about changes in waste composition. Especially cell number three shows higher conductivities but also higher magnetic susceptibility. A strong high conductivity anomaly is seen in the south of cell three (see Fig 16, dotted orange line). These increased conductivities could indicate an elevated metal and/or leachate content. However, it has to be taken into account that the EM data can be influenced by changes of cover layer thickness as well (Dumont et al., 2017). Thus higher amplitudes of the magnetic susceptibility or higher conductivities might not only be caused by a higher content of metallic material for example but might be due to an increased cover layer thickness.

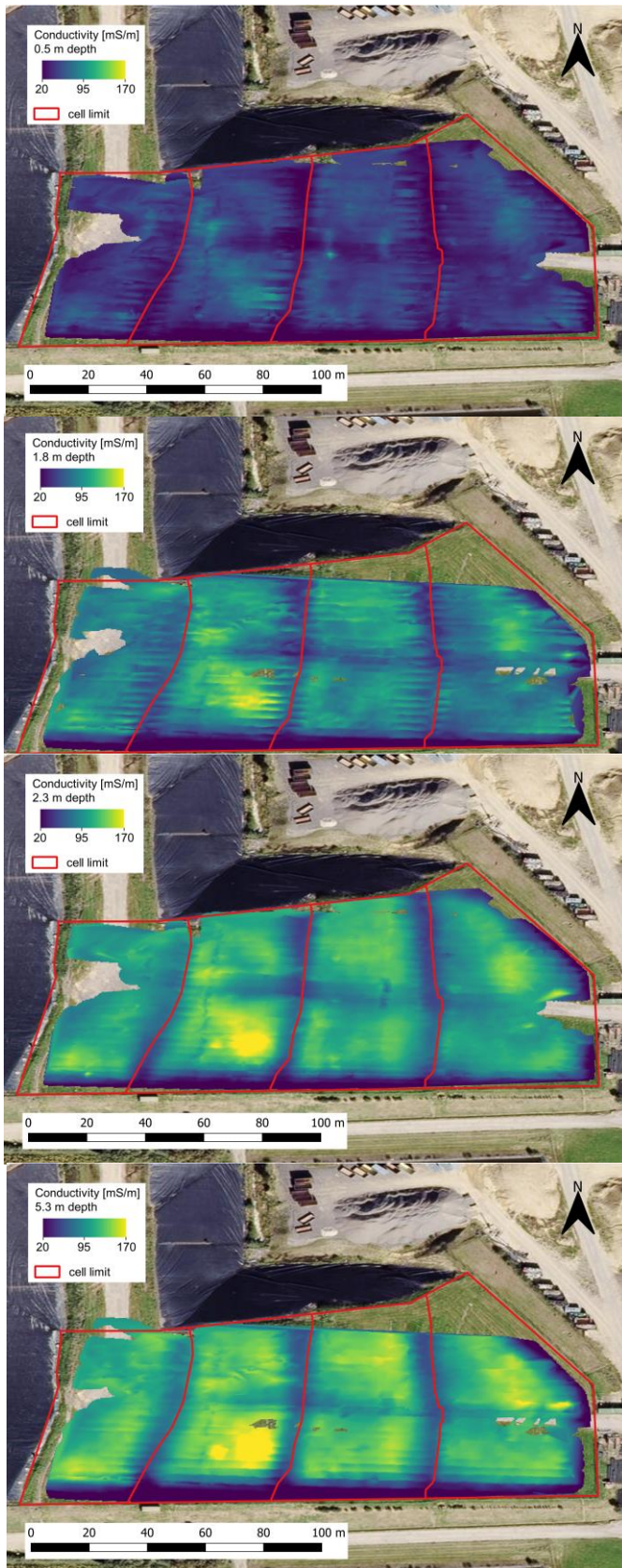


Figure 14: Electrical-conductivity maps derived from the quadrature-phase data measured with the 4 m antenna and horizontal coil alignment. Investigation depth is from top figure to bottom: 0.5 m, 1.8 m, 2.3 m and 5.3 m.

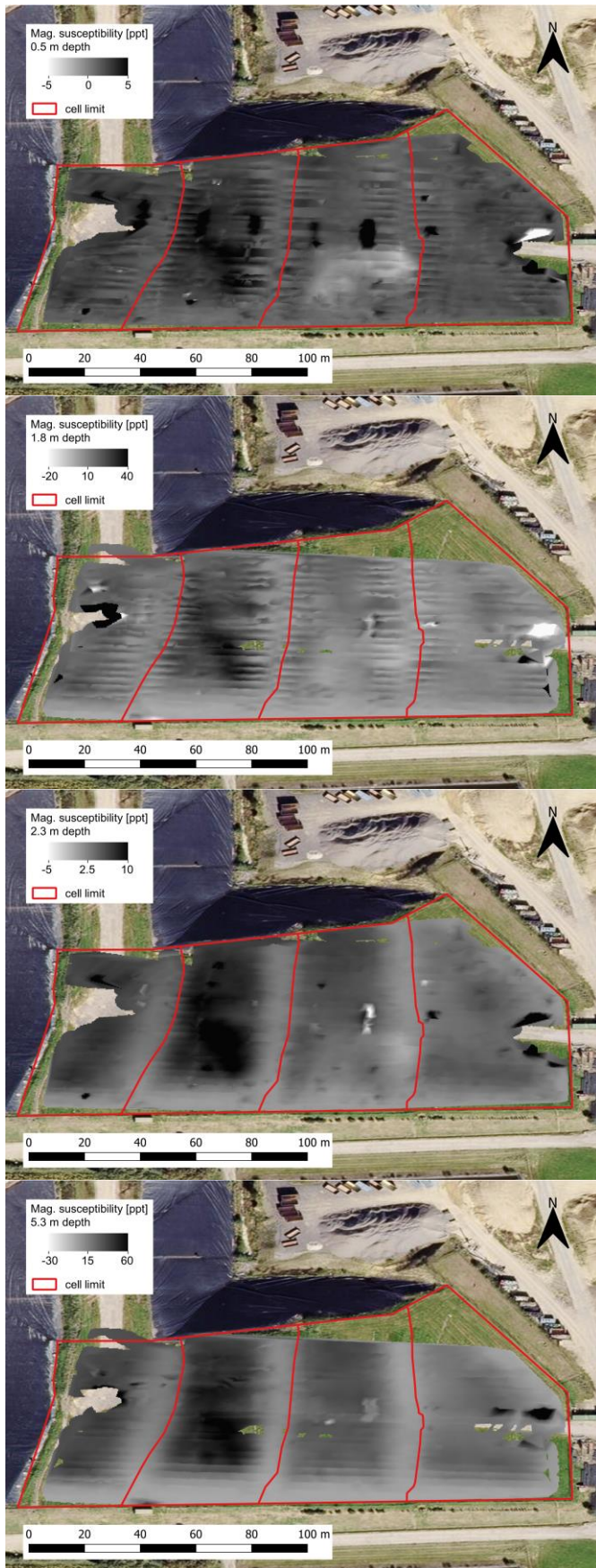


Figure 15: Magnetic susceptibility map derived from the in-phase data measured with the 4 m antenna and horizontal coil alignment Investigation depth is from top figure to bottom: 0.5 m, 1.8 m, 2.3 m and 5.3 m.

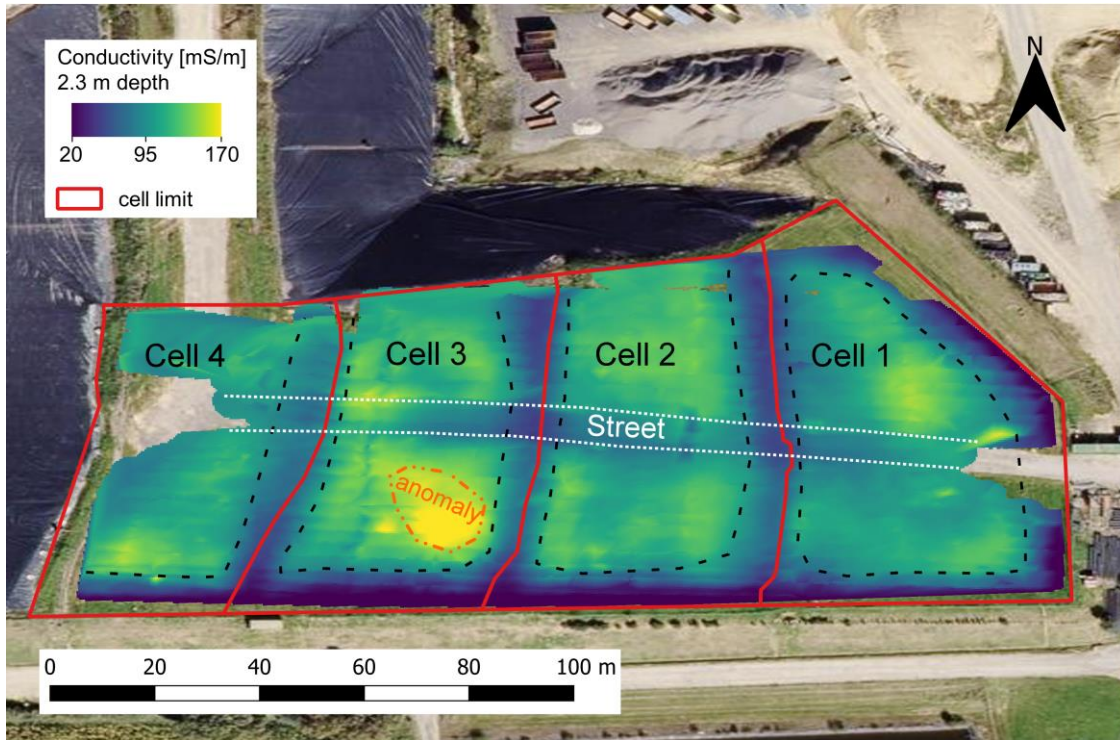


Figure 16: Electrical conductivity at 2.3 m depths. The extent of the waste is clearly visible with the waste having higher conductivities than the separating material which is probably clay (black dashed lines). In addition, the effect of the street is clearly visible (white dotted line). Strong conductivity increase occurs to the South of cell 3 indicating a higher leachate or metallic content.

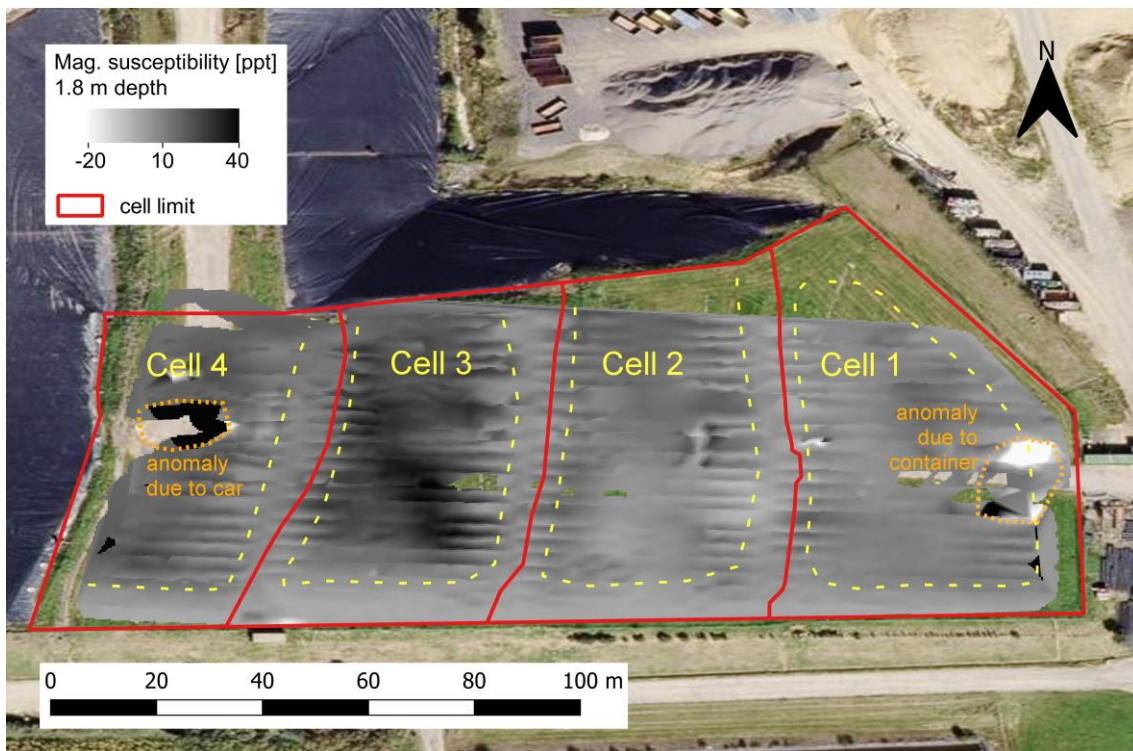


Figure 17: Magnetic susceptibility at 1.8 m depth. Strong anomalies are seen due to nearby metallic infrastructure (orange dotted lines). The magnitude magnetic susceptibility within the cells, especially in cell three, is increased.

Ground Penetrating Radar (GPR)

GPR as a survey technique is limited to the investigation of the near surface. This is because GPR as a method uses relatively high frequencies (generally 10MHz to 2GHz) and that high frequency signals are damped more rapidly when passing through earth materials. Signal damping occurs through processes of attenuation, energy losses at interfaces (transmission & reflection), scattering by particles with dimensions approaching the effective wavelength of the GPR signal, as well as geometrical spreading losses associated with the spherical spreading of the GPR signal. Attenuation is proportional to electrical conductivity, meaning that conductive materials such as clay and water, will serve to increase the attenuation of the GPR signal and therefore reduce the effective depth of investigation. However, GPR data can be rapidly acquired over quite large areas and therefore makes for an excellent reconnaissance technique where shallow structure is expected. In this case the GPR data was collected to investigate potential variation in the thickness of the cover layers over the waste. The very high conductivity of the waste material is expected to cause very strong signal attenuation. Therefore, we do not expect to retrieve any information about the waste material.

The GPR data was processed and interpreted using the REFLEX-Win software package (Sandmeier Geophysical Research). Processing undertaken was minimal, but after the importing and georeferencing the data profiles, included removal of temporally consistent background noise and bandpass filtering to reduce noise at frequencies significantly above and below the central frequency of the GPR antenna used (250MHz). Figure 18 presents two interpreted GPR profiles which have also had topography added.

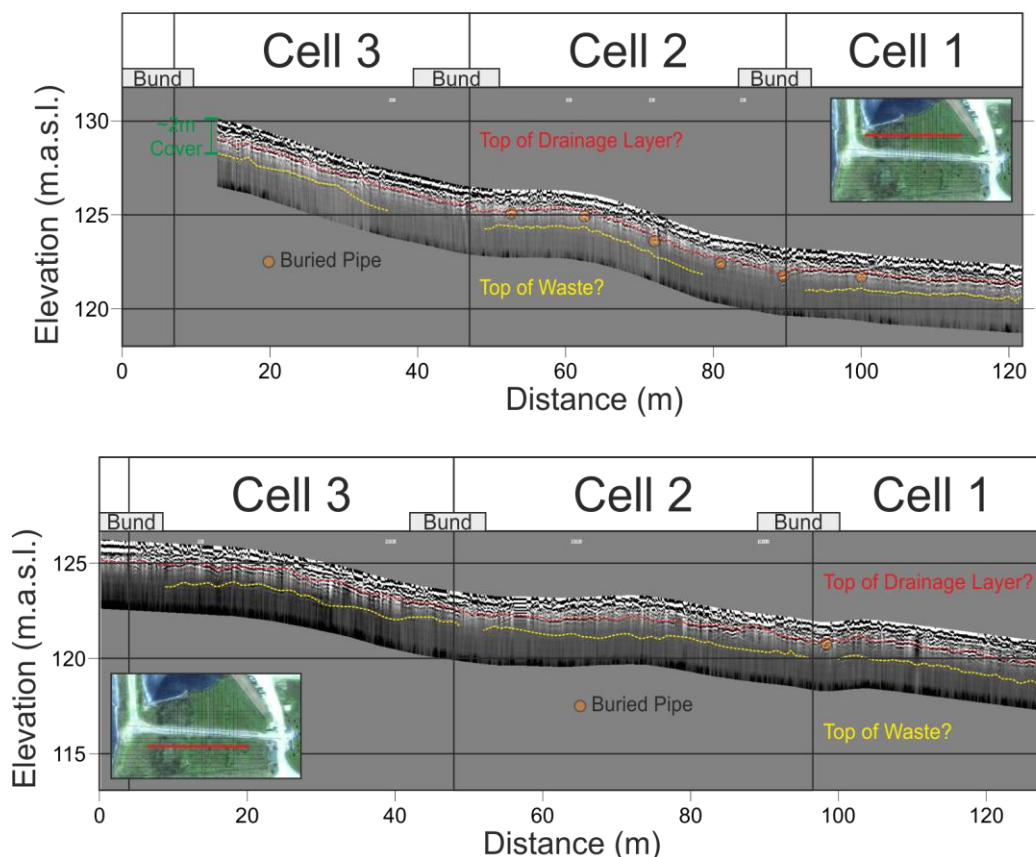


Figure 18: Examples of processed GPR profiles with topography added. Upper profile located to the north of the access road cutting across the site, whilst the lower profile is located to the south of the access road.

Whilst very little information is observed at depths in excess of 2m below the surface, some distinct and laterally continuous layering is noted in the near surface, which is interpreted to relate to the engineered capping layers located above the waste. Two horizons have been identified. The first, highlighted in red in Figure 18, is interpreted to relate to the base of the soil capping, where a geotextile rests on a drainage layer (see Fig. 19). This interpretation is based on the observation of a number of buried pipes just beneath the picked interface (highlighted with orange dots), which do not relate to any of the leachate / biogas pipes and are therefore considered likely to be drainage pipes running north-south (down-slope) across the site.

The second (deeper) interface (identified in yellow) is less-well defined across the survey area, but generally is quite consistent laterally. Given that the engineered capping is expected to be of the order of 2m in thickness across the site, assuming an average velocity of 0.12m/nS, this interface is therefore assumed to be related to the top of the actual waste as indicated in Figure 19. It is noted that the apparent gaps in this interface correspond to the banded areas between waste cells. The two interfaces have been interpolated for the area to the south of the access road in order to complement the EM and magnetic surveys (Fig. 20). Generally, there is a tendency that the capping layer is thicker towards West as seen on Figure 20 (bottom). Patches of thinner coverlayer thickness are seen on the three eastern cells (cells no 1 to 3).

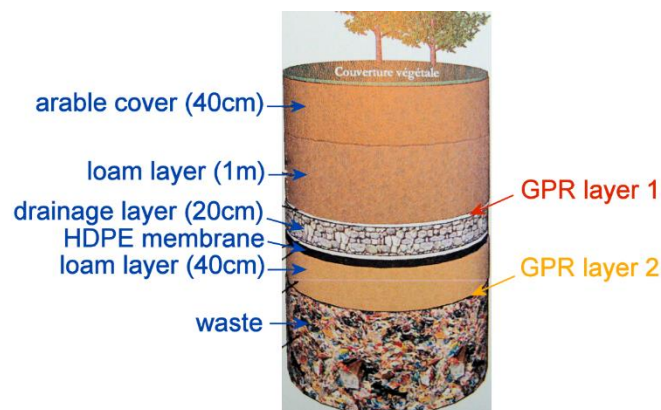


Figure 19: Schematic figure of the capping layer structure. The interfaces identified with GPR are marked in red and yellow.

Figure 21 compares the capping layer thickness found by GPR (deeper interface) with the EM data. For the EM measurements, higher electrical conductivities can be caused by changes in waste composition (e.g. higher metal content or higher leachate content) but also by a thinner capping layer. The capping layer thickness gained through the GPR measurements can therefore help to improve the interpretation of the EM data. Figure 21 shows a tendency that areas with thinner capping relate to higher conductivities meaning that the higher conductivities could be partially caused by a thinner capping. However, at the very high conductivity anomaly in cell no 3 (compared with Fig. 16), the layer thickness is not particularly thin. This indicates that the anomaly is rather caused by the waste composition/leachate content than the capping layer thickness.

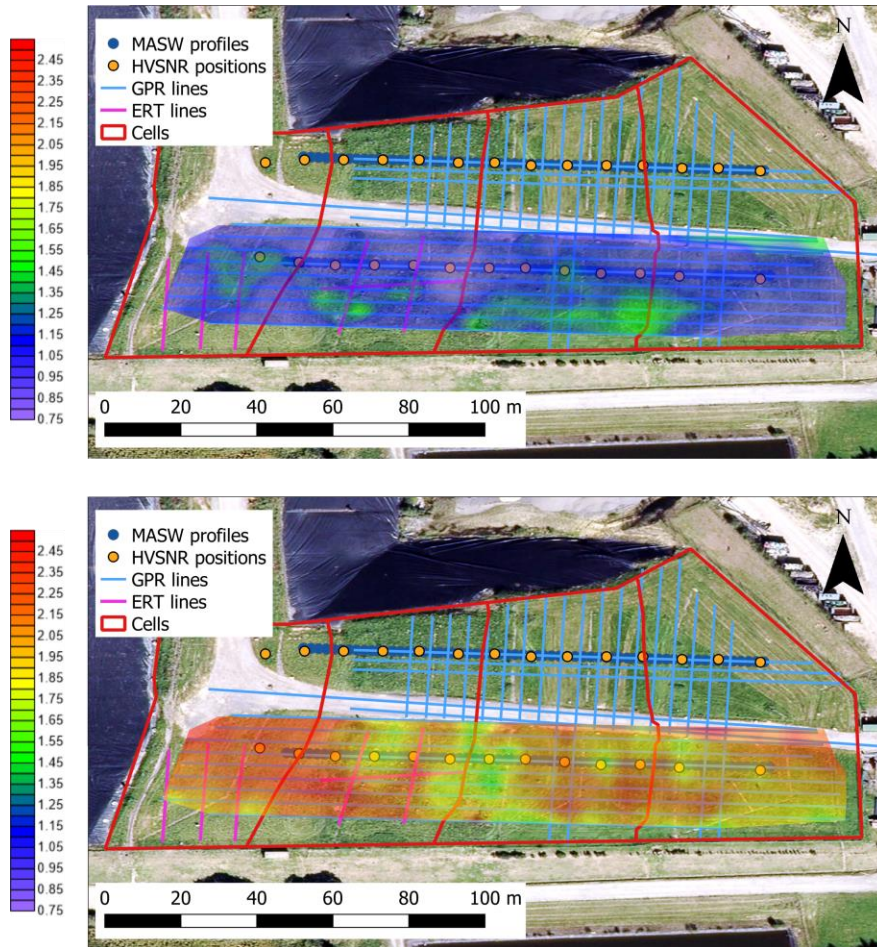


Figure 20: Interpolated surfaces corresponding to the base of soil capping layers (upper) and top of waste (lower) as observed from the GPR data collected to the south of the access road. Colour scale relates to depth below the surface (in metres).

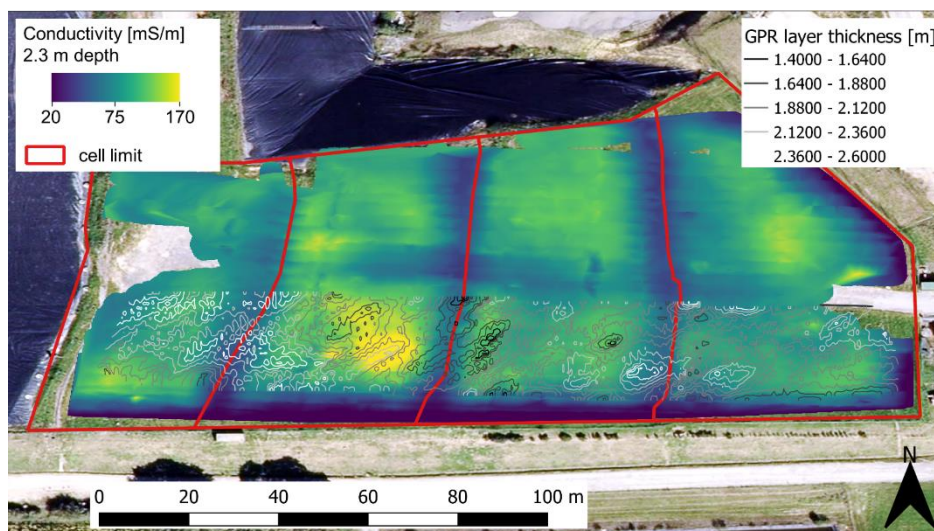


Figure 21: Comparison of the capping layer thickness retrieved from the GPR measurements (deeper interface, displays as contour plot) with the conductivity map gained through the EM measurements.

HVSNR

The aim of this technique -popularized by Nakamura (1989)- is to estimate the natural frequency of soft soils when there is a large impedance contrast with the underlying bedrock (SESAME European research project). For this purpose, we acquired 3-component ambient noise recordings (vertical, north-south and east-west directions) in 14 stations equally spaced along the northern and southern MASW profiles (Fig. 6).

For each station, the following process was done using the software GEOPSY:

1. Selection of the N most stationary windows in the 3 components
2. Computation of Fourier amplitude spectra for each time windows (+ smoothing)
3. Average of horizontal components
4. Computation of N horizontal/vertical components ratios (H/V)
5. Computation of the average H/V ratio

The frequency where the higher amplitude of the H/V ratio is shown, corresponds to the resonance frequency f_0 of the underlying soil (see example in Fig. 22). Most of the H/V spectra presented more than one high amplitude peak at different frequencies that could be originated by vibrating sources or human activities. To visualize the lateral variations of f_0 along the seismic profiles we interpolate the H/V amplitude spectra of all stations and plotted the frequency range vs. distance along the profile (see Figs. 23 and 24). In the southern profile, there is a continuous high H/V amplitude zone between 2 and 3 Hz that corresponds to the f_0 values of the waste cells. On the other hand, there is a more variable zone in the northern profile, going from 2.5 Hz at the origin, to 4 Hz at the end of the profile. For both profiles there is a background high H/V amplitude at short frequencies that could be associated with wind.

Furthermore, for a 1D geology, the resonance frequency depends on the S-wave velocity (β) and the thickness of the uppermost soft layer (H) according to

$$f_0 = \frac{\beta}{4H}$$

Using this relationship and the previous MASW results we calculated the thickness of the soil layer H, i.e. the thickness of the waste body if there is high impedance contrast enough. Figures 25 and 26 show the topography and the estimated bottom limit of the waste from then southern and the northern profiles using a velocity of 100 m/s, which agrees with the 10 m thickness of the cell waste. Finally, for both profiles, the lower limit of the waste cells follows the trending of the topography and only minor subsidence anomalies can be seen.

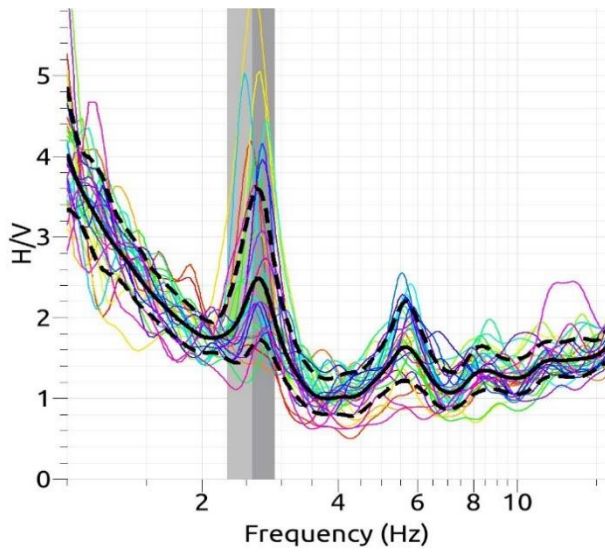


Figure 22: H/V average ratio for one station along the first MASW profile. The grey band indicates the highest H/V value at the resonance frequency $f_0 = 2.68$ Hz

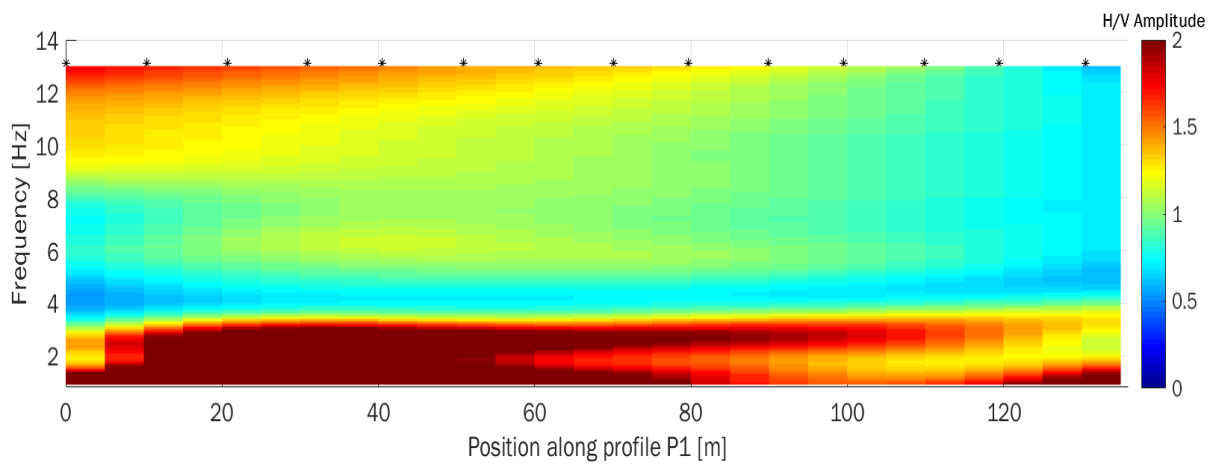


Figure 23: Interpolation of H/V amplitude spectra along profile P1. The black dots represent the location of seismic stations.

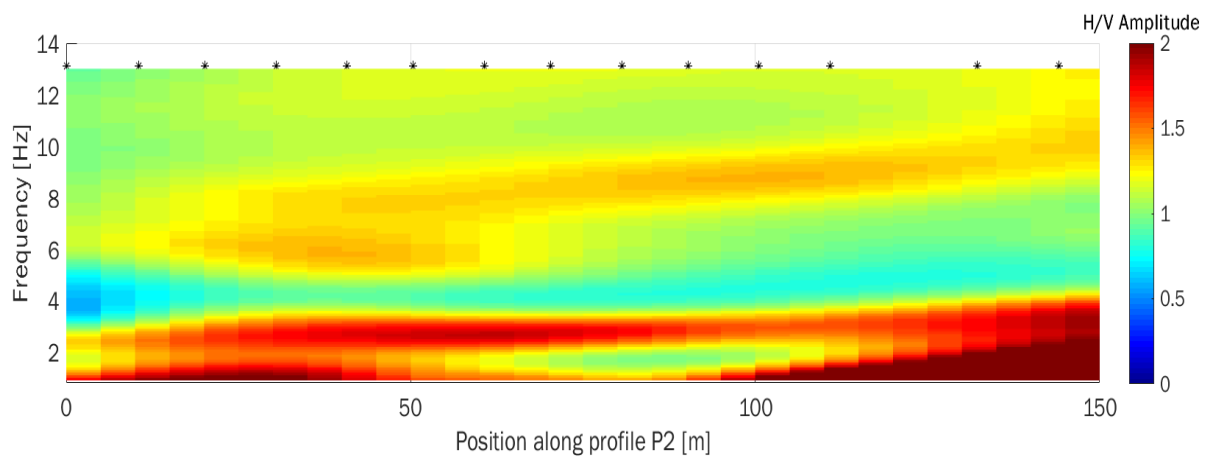


Figure 24: Interpolation of H/V amplitude spectra along profile P2. The black dots represent the position of recording stations.

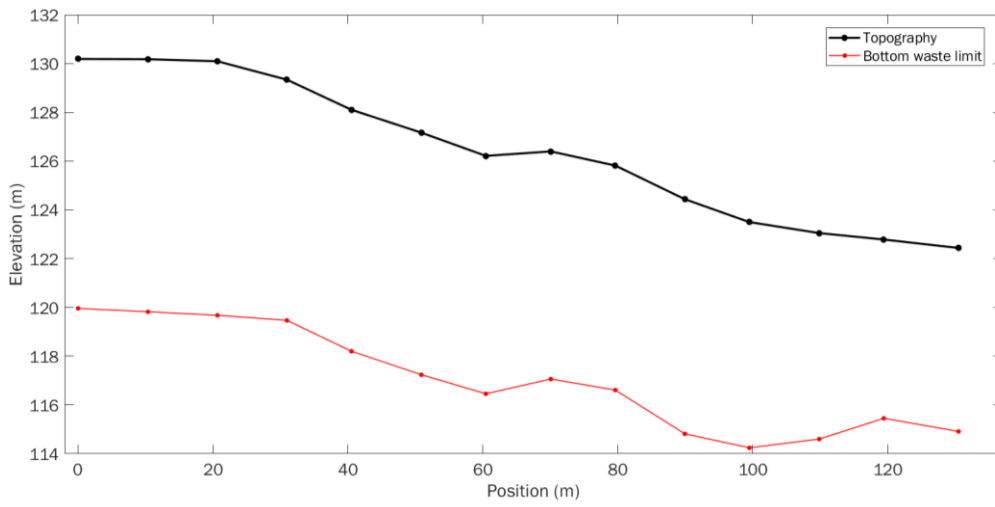


Figure 25: Topography and bottom waste limit in red for profile 1, along the West-East direction.

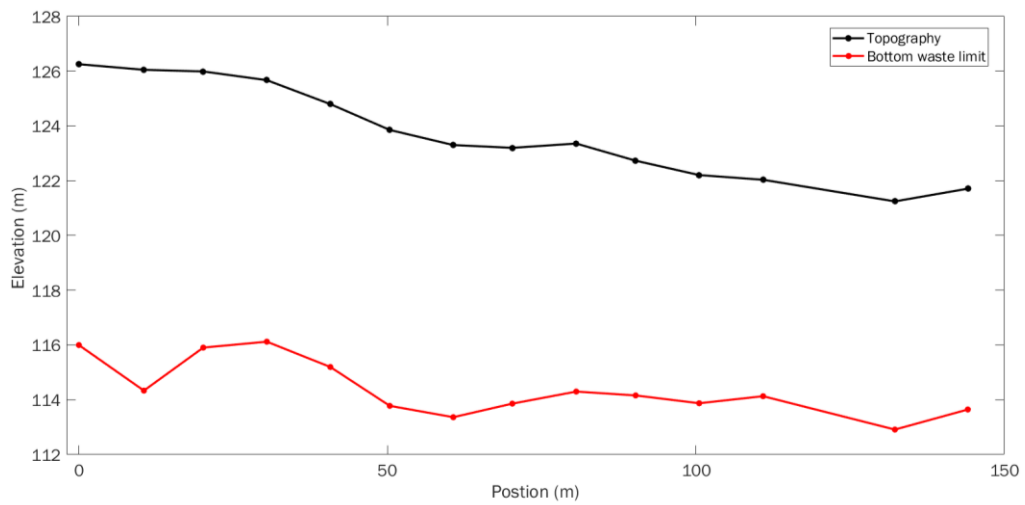


Figure 26: Topography and bottom waste limit in red for profile 2, along the West-East direction

MASW

MASW surveys use the seismic field records gathered using the same receiver array configuration adopted in shallow seismic refraction and reflection surveying (Park et al., 1999). Rather than using the body waves produced from a seismic source however, MASW uses the seismic wave energy propagating as Rayleigh waves, which accounts for approximately two thirds of the total energy imparted by the source (Gunn et al., 2012; Richart et al., 1970). Rayleigh waves are observed as the ground surface roll that radiates from the vertical impact and are utilised in surface wave surveys to approximate the shear wave velocity, which is approximately 1.1 times the Rayleigh wave velocity and is controlled by the small strain stiffness and density of the soil (Gunn et al., 2006; Richart et al., 1970). Rayleigh waves are dispersive; that is, the velocity of wave propagation, called the phase velocity, varies with frequency. The wavelength (and therefore depth of investigation) associated with each frequency also therefore differs, and in this manner, field survey methods that propagate multi-frequency Rayleigh waves form the basis of a shear wave velocity and stiffness ground imaging method.

The maximum investigation depth for MASW is considered to be about half of the wavelength of the lowest recorded surface wave frequency (e.g. Dumont et al., 2017; Park et al., 1999). Thus, using relatively low frequency (4.5Hz) geophones should increase the depth of investigation. In order to undertake MASW processing, shots were acquired along the profiles indicated in Figure 8, with the streamer moved a distance of 2m along the line for each successive shot. The MASW data was processed using the SurfSEIS software (Kansas Geological Survey (KGS)). Each shot record was transformed to calculate the phase velocity-frequency distribution, also known as a dispersion curve and the fundamental mode of each dispersion curve was then picked. From the dispersion curves two methodologies (approximate and inversion) were used to construct shear wave velocity profiles and the results of each of these methods are displayed in Figures 27 and 28 below.

The approximated velocity profile (upper images in Figs. 27 and 28), is constructed using a depth equivalent to a fraction of the Rayleigh wavelength (Foti and Fahey, 2003; Joh, 1996), with one third of the wavelength often used because a significant proportion of the particle motion in the ground associated with Rayleigh wave propagation is approximately at this depth (Gunn et al., 2006; Joh, 1996; Richart et al., 1970). Vertical 2D sections were then constructed along each profile by interpolating between each 1D velocity profile. This approach is highly suited to situations where the structure is predominantly sub-horizontal and planar, but will be less effective in resolving rapid lateral changes in seismic velocity and velocity inversions.

The dispersion curves were also inverted to produce a series of 1D depth-velocity models, based on the iteration of a 10-layer starting model. This was undertaken using the SurfSEIS processing software (KGS), and the individual profiles were interpolated to produce continuous 2D sections (lower images in Figs. 27 and 28). Whilst this produces models of apparently increased detail, it is important to note that as for any modelling procedure, all solutions are non-unique and therefore the plausibility of any model produced should be evaluated using any other available information.

Irrespective of the modelling procedure applied, the areas of waste appear to be characterised by very low shear wave velocities of less than 120 m.s^{-1} , with the approximated profiles indicating that the lowest velocities are observed in the centre of the individual cells. The banded areas separating the cells appear to correspond to higher velocities at the surface, but only in the modelled profile to the south of the access road is there any evidence of a sloped, increased velocity structure observed.

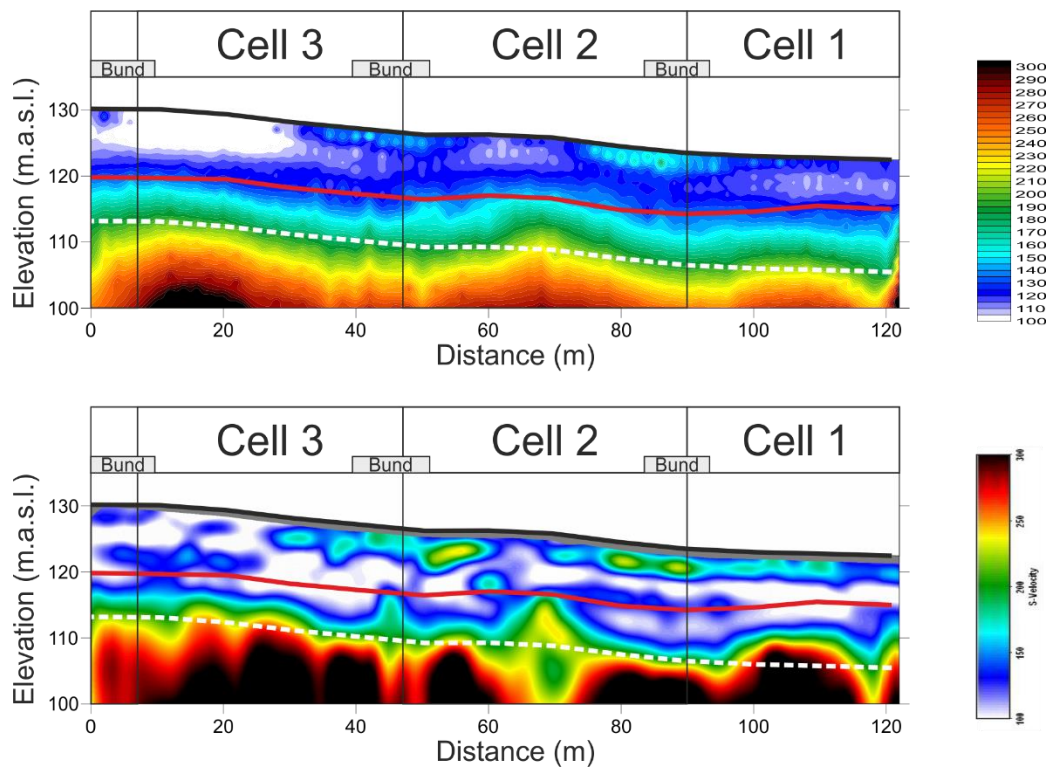


Figure 27: 2D shear wave velocity profiles constructed for the MASW line acquired to the north of the access road (W-E oriented, see Figure 8). Upper-Approximated velocity profile assuming an investigation depth equal to 1/3 of the wavelength of the Rayleigh wave. Lower-Inverted velocity profile derived using a 10 layer starting model and varying thickness of layers. Solid red line represents the interface corresponding to the top of bedrock identified using the HVSNR technique. Dashed white line indicates the maximum thickness of waste expected at site (17m below the surface).

Two interfaces are indicated on each of the velocity profiles presented in Figures 27 & 28. The upper (solid red) line represents the interface interpreted to relate to the base of the waste materials from the HVSNR data. This interface shares a very similar morphology to the approximated MASW velocity profiles, corresponding to velocities of 130-150 m.s⁻¹. A similar relationship is noted from the modelled velocity sections, except to the north of the access road (Figure 27), where the interface appears to correspond to an intermediate layer that appears to separate two low velocity layers. This high velocity layer corresponding to the HVSNR interface may represent an intermediate layer of increased compaction, possibly where increased thicknesses of waste have been deposited, in order to reduce the potential for settlement across these areas. Intrusive sampling, however, would be required to A)-prove if this is a real feature, or B)-to characterise what this feature is constructed from.

The white dashed line indicates the maximum thickness of waste expected across the site, which is 17m beneath the surface (2m of cover materials plus a maximum of 15m of waste). This corresponds to a velocity of 190-230m.s⁻¹ on all of the velocity profiles presented except for the modelled section to the south of the access road, where the base of the waste (or top of bedrock) appears to form a less regular surface than observed to the north of the access road, where the greatest thickness of waste is observed from the MASW data.

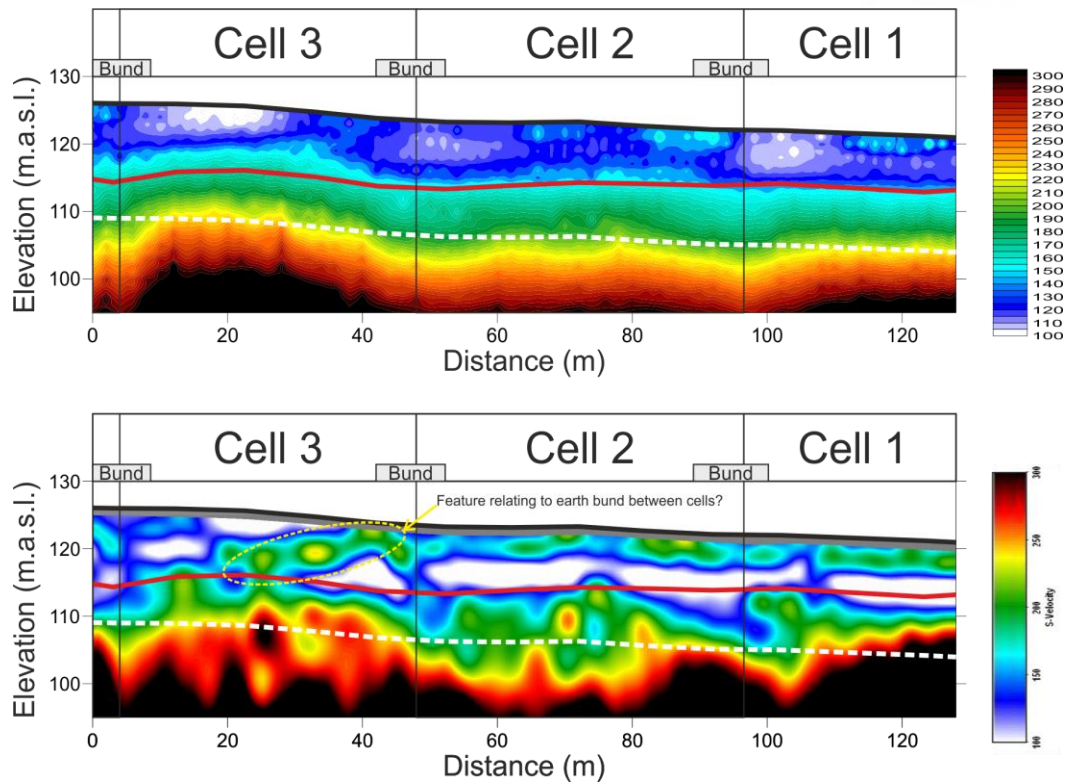


Figure 28: 2D shear wave velocity profiles constructed for the MASW line acquired to the south of the access road (W-E oriented, see Figure 8). Upper-Approximated velocity profile assuming an investigation depth equal to 1/3 of the wavelength of the Rayleigh wave. Lower-Inverted velocity profile derived using a 10 layer starting model and varying thickness of layers. Solid red line represents the interface corresponding to the top of bedrock identified using the HVSNR technique. Dashed white line indicates the maximum thickness of waste expected at site (17m below the surface).

Very low velocities are noted to extend up to the surface of Cell 3, which corresponds to the most recent injection of leachate undertaken at the time of the survey. This suggests that a much higher moisture content in this cell (compared to the other cells), has resulted in a measurable reduction in the shear strength of the waste materials.

The shear wave velocity of the undisturbed bedrock across the site appears to $>250 \text{ m}\cdot\text{s}^{-1}$.

ERT and IP

In Figure 27, we show 3D ERT and IP models that were kindly provided by S. Moreau from IRSTEA. Presented models refer to data collected in January 2019, i.e. 2 months after the geophysical survey carried out in the scope of RAWFILL. Trenches filled with sand where the electrodes were buried are clearly visible both in resistivity and phase models. A rippling pattern close to the electrodes is also observed and is related to a common inversion artefacts. More interestingly, we observe a lower electrical resistivity in cell 3 than in cell 4 (mean value of 3.9 Ohm.m against 5.9 Ohm.m) which is consistent with the electrical conductivity maps obtained with the EM method. On average, not much difference is observed in terms of phase between the two cells (mean value of 18.8 mrad in cell 3 and 19.3 mrad in cell 4). Figure 28 shows two transects in the 3D models. We observe lower electrical resistivity in the southern and lower part of each cell which is consistent again with the EM results and might indicate a higher leachate/water content. However, such difference might also be attributed to a difference of model sensitivity (Fig. 28C) which is as expected much lower in the northern part of the cells where no electrodes are buried. In the zones where the sensitivity is high, we nevertheless observe a decrease of electrical resistivity with depth which was also observed on the EM conductivity maps.

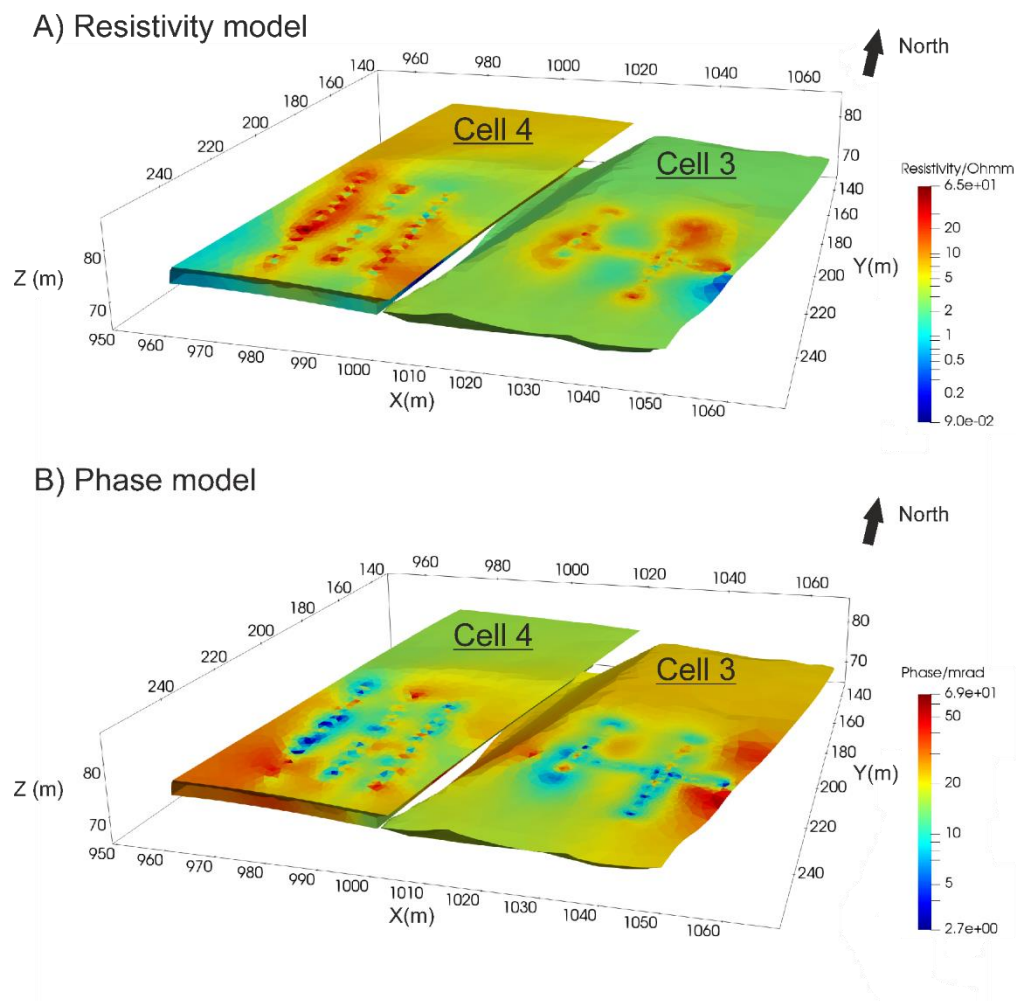
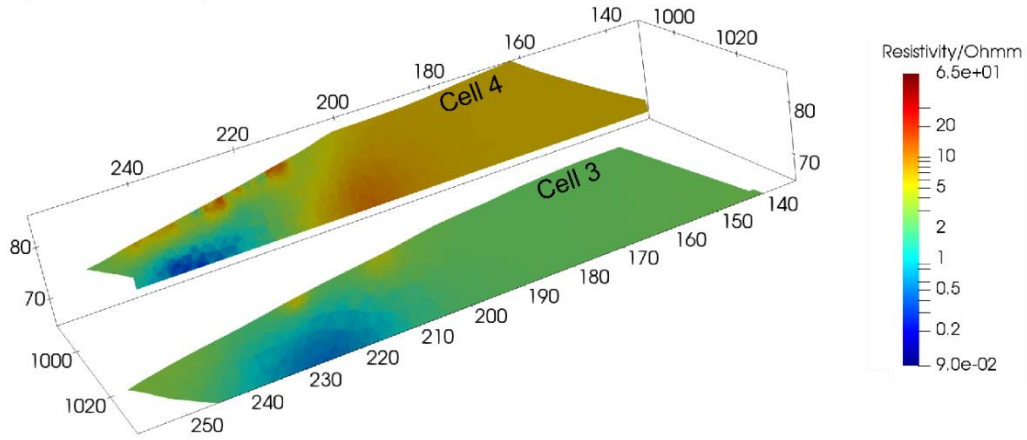
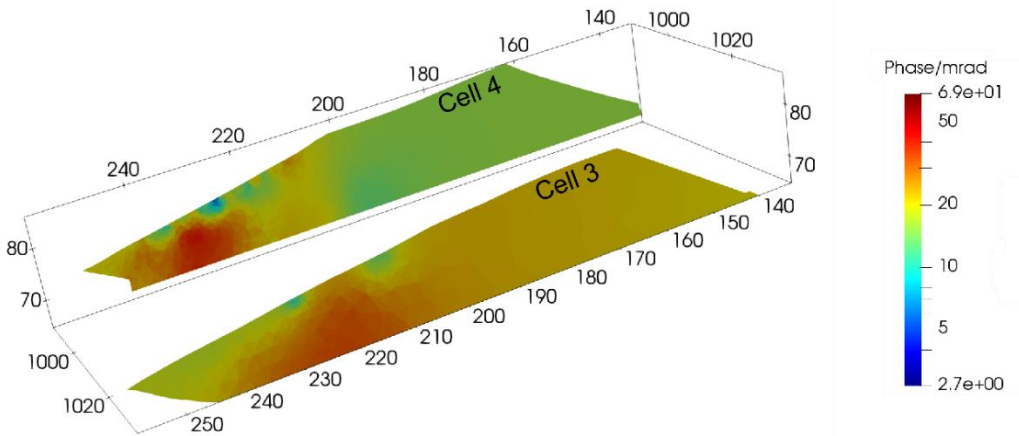


Figure 29: 3D representation of cells 3 and 4 with A) resistivity model and C) phase model.

A) Resistivity model at X = 987 m and 1034 m



B) Phase model at X = 987 m and 1034 m



C) Model sensitivity at X = 987 m and 1034 m

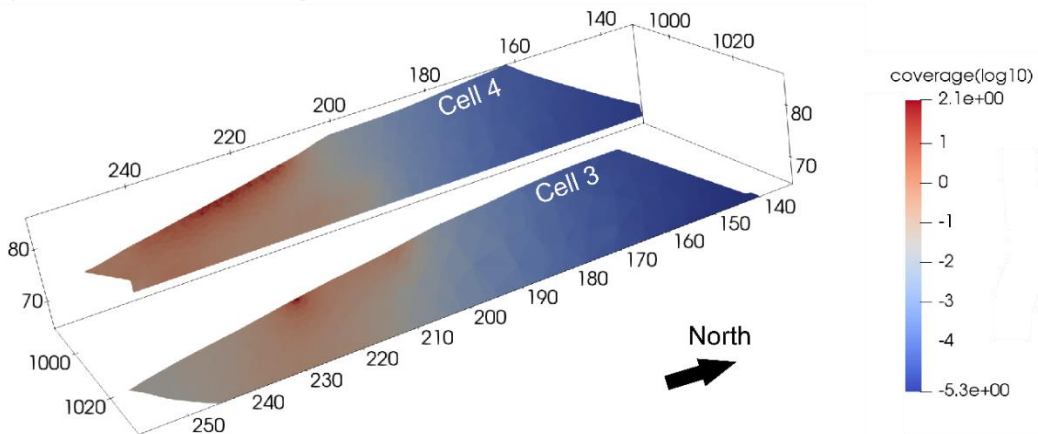


Figure 30: Transects of electrical resistivity (A), phase (B) and model sensitivity (C) at X=987 m (cell 4) and 1034 m (cell 3).

Conclusion

Selected geophysical methods allowed to identify several interesting features on the Les Champs Jouault site. Magnetometry mapping results made it possible to detect buried metallic structures below the road. They also showed an overall increase of magnetic from east to west that is attributed to a greater thickness of waste. Electromagnetic mapping highlighted the presence of more electrically conductive areas, either related to a thicker cover layer (as shown by the GPR profiles) or to higher leachate/water saturation (as also confirmed with ERT results). With regards to the depth to the natural soil, only seismic methods proved effective providing consistent depth in relation to the available information. Geophysical results presented in this report will serve to produce a sampling plan (Deliverable I2.3.1). Ground truth data that will be collected (Deliverable I2.3.3) will then be used to validate geophysical data and establish correlations (Deliverable I2.3.4) for the construction of a resource distribution model.

References

- Audebert, M., 2015. Développement d'une méthode de contrainte des modèles hydrodynamiques par une stratégie d'analyse des données géophysiques ERT: Application aux écoulements de lixiviat dans les massifs de déchets', Grenoble Alpes.
- Audebert, M., Clément, R., Grossin-Debattista, J., Günther, T., Touze-Foltz, N., Moreau, S., 2014. Influence of the geomembrane on time-lapse ERT measurements for leachate injection monitoring. *Waste management*, 34: 780-90.
- Audebert, M., Clement, R., Moreau, S., Duquennoi, C., Loisel, S., Touze-Foltz, N. 2016. Understanding leachate flow in municipal solid waste landfills by combining time-lapse ERT and subsurface flow modelling - Part I: Analysis of infiltration shape on two different waste deposit cells. *Waste Management*, 55: 165-75.
- Dumont, G., Robert, T., Marck, N., Nguyen, F. 2017. Assessment of multiple geophysical techniques for the characterization of municipal waste deposit sites. *Journal of Applied Geophysics*, 145: 74-83.
- Foti, S., Fahey, M., 2003. Applications of multistation surface wave testing. *Deformation Characteristics of Geomaterials*: 13-20.
- Grossin-Debattista, J., Clement, R., Bouchez, T., Mazeas, L., Moreau, S. 2014. Suivi et optimisation de l'ISDND de la SAS Les Champs Jouault exploitée en mode bioréacteur: Rapport final du projet. In: 242. IRSTEA, centre d'Antony.
- Gunn, D.A., Nelder, L.M., Jackson, R.D., Northmore, K.J., Entwisle, D.C., Milodowski, A.E., Boardman, D.I., Zourmpakis, A., Rogers, C.D., Jefferson, I., Dixon, N. 2006. Shear wave velocity monitoring of collapsible loessic brickearth soil. *Quarterly Journal of Engineering Geology and Hydrogeology*, 39: 173-88.
- Gunn, D.A., Williams, G., Raines, M.G., Busby, J.P., Williams, J.D.O, Pearson, S.G. 2012. Comparison of surface wave techniques to estimate shear wave velocity in a sand and gravel sequence: Holme Pierrepont, Nottingham, UK. *Quarterly Journal of Engineering Geology and Hydrogeology*, 45: 139-60.
- Günther, T., Rücker, C., Spitzer, K.. 2006. Three-dimensional modelling and inversion of DC resistivity data incorporating topography — II. Inversion. *Geophysical Journal International*, 166: 506-17.
- Joh, S.H. 1996. Advances in the Data Interpretation Technique for Spectral Analysis of Surface Waves Measurements. *PhD thesis, University of Texas, Austin, TX, USA. 240p.*
- Jouen, T. 2018. Caractérisation de l'évolution de l'état de biodégradation des massifs de déchets non dangereux en post-exploitation: Application de méthodes géophysiques. *PhD thesis*, Institut agronomique, vétérinaire et forestier de France, Paris, France.
- Park, C.B., Miller, R.D., Xia, J.H. 1999. Multichannel analysis of surface waves. *Geophysics*, 64: 800-08.
- Richart, F., Hall E., Woods, R.D. 1970. Vibrations of soils and foundations. Prentice-Hall: Englewood Cliffs ; Hemel Hempstead.
- Rücker, C., Günther, T., Spitzer, K. 2006. 3-d modeling and inversion of DC resistivity data incorporating topography—Part I: Modeling. *Geophysical Journal International*, 166: 495-505.

Contact

Feel free to contact us.

Local contact details:

BELGIUM	ATRASOL Cleantech Flanders / VITO OVAM SPAQuE Université de Liège	renaud.derijdt@atrasol.eu alain.ducheyne@vito.be ewille@ovam.be c.neculau@spaqua.be f.nguyen@ulg.ac.be
FRANCE	SAS Les Champs Jouault	champsjouault@gmail.com
GERMANY	BAV	pbv@bavmail.de
THE UK	NERC	jecha@bgs.ac.uk

Coordination office:

BELGIUM	SPAQuE Boulevard Maurice Destenay, 13 4000 Liège	c.neculau@spaqua.be
----------------	--	---------------------
